







Cite this: *Nanoscale*, 2019, **11**, 21302

N,S–Codoped hierarchical porous carbon spheres embedded with cobalt nanoparticles as efficient bifunctional oxygen electrocatalysts for rechargeable zinc–air batteries†

Xiaojing Zhu, ^a Jiale Dai, ^a Ligui Li, ^{*a,b,c} Zexing Wu ^d and Shaowei Chen ^{*a,e}

Rational design and fabrication of cost-effective, efficient bifunctional electrocatalysts is fundamentally important for the air cathode of metal–air batteries. Herein, a Co(II) ion-driven self-assembly strategy is described for the synthesis of cobalt-based nanostructured transition metal compounds (Co-NTMCs) embedded in nitrogen and sulfur codoped hierarchical porous carbon submicrospheres (Co-NTMCs@NSC), where condensation of thiourea-ethylenediamine-formaldehyde resin (TEFR) is induced by Co(II) ions which is simultaneously assembled with polydopamine to form a multifunctional precursor through coordinated interaction. The resulting Co-NTMCs@NSC sample comprises abundant hierarchical porous textures, a high content of active cobalt species including the nanoparticles of Co, Co₃O₄ and amorphous CoS_x, and a considerable amount of defective structures. These characteristics lead to remarkable oxygen electrocatalytic activities, with a half-wave potential of +0.833 V vs. RHE, which is comparable to that of commercial Pt/C for the oxygen reduction reaction (ORR), and a lower overpotential of 284 mV than RuO₂ at 10 mA·cm⁻² for the oxygen evolution reaction (OER) in alkaline media. Furthermore, its operational stability is also much higher than that of commercial RuO₂ and Pt/C catalysts. When used as a breathing air electrode for Zn–air batteries, Co-NTMCs@NSC shows a higher open-circuit voltage (1.509 V), higher discharge power density (262 mW cm⁻²) and better charge–discharge reversibility than commercial Pt/C. The results from the present work suggest that controlled assembly of functional polymers may be exploited for the preparation of doped carbon/metal nanoparticle nanocomposites as viable, high-performance catalysts for electrochemical energy technologies.

Received 4th September 2019,
Accepted 8th October 2019

DOI: 10.1039/c9nr07632h

rscl.li/nanoscale

Introduction

Fuel cells and metal–air batteries represent two new-generation energy conversion technologies that feature many

advantages, such as high energy-conversion efficiency and zero or low emission of pollutants, and hence they are considered as potential alternative technologies to solve the current environmental issues and energy crisis.^{1–4} However, these devices usually suffer from serious limitations due to the kinetically sluggish oxygen reduction reaction (ORR) and oxygen evolution reaction (OER).^{5–9} Although the kinetic process can be significantly promoted by noble-metal-based (*e.g.*, Pt, Ru, Ir, and alloys) electrocatalysts, their high cost and poor durability and susceptibility to fuel crossover severely hinder their widespread commercial applications.^{10–12} Therefore, it is of great significance to develop advanced electrocatalysts with high efficiency, low cost and excellent durability.

Heteroatom-doped carbon materials have been considered as viable alternatives, owing to the ease of realizing high surface area, large pore volume, excellent electrical conductivity, low cost, and highly tunable composition.¹³ To date, doping carbon materials with single or multiple heteroatoms (*e.g.*, N, S, P and B) has been proven to be effective in altering the electronic structure and successfully promoting the ORR/

^aNew Energy Research Institute, School of Environment and Energy, South China University of Technology, Guangzhou Higher Education Mega Centre, Guangzhou, 510006, China. E-mail: esguili@scut.edu.cn

^bKey Lab of Pollution Control and Ecosystem Restoration in Industry Clusters, Ministry of Education, South China University of Technology, Guangzhou 510641, China

^cState Key Laboratory of Polymer Physics and Chemistry, Changchun Institute of Applied Chemistry, Chinese Academy of Sciences, Changchun 130022, China

^dState Key Laboratory Base of Eco-chemical Engineering, College of Chemistry and Molecular Engineering, Qingdao University of Science & Technology, No. 53 Zhengzhou Road, 266042 Qingdao, China

^eDepartment of Chemistry and Biochemistry, University of California, 1156 High street, Santa Cruz, California 95064, USA. E-mail: shaowei@ucsc.edu

†Electronic supplementary information (ESI) available: Photograph, FTIR spectra, XPS spectra, SEM images, EDS spectra, TGA curve, Raman spectra, LSV curves of carbonaceous nanomaterials, and K–L plots. See DOI: 10.1039/c9nr07632h

OER electrocatalytic activity.^{10,14} A number of structural defects are also concurrently generated during the doping process, leading to further improvement of the electrocatalytic activity.¹⁵ Additionally, nanostructured transition metal compounds (NTMCs), for example, transition metal oxides or sulfide nanoparticles, have also been reported to be active in ORR or OER electrocatalysis. Of these, Co-containing nanomaterials are the most widely used transition-metal electrocatalysts for the ORR and OER, such as metallic Co and multiple Co-N_x-C_y species in Co, N codoped carbons for the ORR,¹⁶ Co₃O₄ for the ORR and OER,¹⁷ and CoS_x for the OER.¹⁸ Hence, one straightforward strategy to prepare efficient, durable bifunctional electrocatalysts for the ORR and OER is to combine active NTMCs with heteroatom doped porous carbon matrices.

High-temperature pyrolysis is a general route to dope heteroatoms into carbon matrices.^{19,20} Thiourea is usually used as a source of S and N dopants.²¹ Unfortunately, the thus-obtained doped carbon typically exhibits a predominantly microporous architecture, which severely limits the diffusion coefficient of reactants and impedes the accessibility of interior active sites. Very recently, Hyeon *et al.* have demonstrated that mesopores contribute to electrolyte wetting of the physical surface area and increase the portion of electrochemically available active sites, while macroporous structures promote kinetic accessibility to the available active sites.²² Thus, generating hierarchical porous architectures with abundant meso and macro-pores as well as concurrent embedment of active Co-NTMCs is of great significance in the design of high-performance electrocatalysts.

Herein, we describe a novel Co(II) ion-driven self-assembly strategy for the synthesis of nitrogen and sulfur co-doped hierarchical porous carbon spheres that were embedded with cobalt-containing NTMCs (Co-NTMCs@NSC). In this strategy, the precursor was prepared by self-polymerization of dopamine and its simultaneous assembly with thiourea-ethylenediamine-formaldehyde resin (TEFR) induced by the coordination of thiol groups with Co(II) ions (which acted as mediators). After carbonization, the materials exhibited a hierarchical structure with rich mesopores and macropores that originated from the pyrolysis of the Co-TEFR precursor, a unique feature that was anticipated to facilitate electrolyte infiltration and promote kinetic accessibility of the active sites. Significantly, the synthetic protocol does not require additional hybrid dopants *via* multi-step reactions or need extra pore-forming reagents, and can be easily applicable for the synthesis of other NTMC-based hybrid structures. With a hierarchical porous structure and abundant structural defects and active Co-containing species, the as-synthesized Co-NTMCs@NSC composites displayed a large specific surface area and high catalytic activity towards the ORR/OER, with a half-wave potential of +0.833 V for the ORR and a low overpotential of 284 mV at 10 mA cm⁻² for the OER in alkaline medium. An assembled Zn-air battery (ZAB) with the Co-NTMCs@NSC catalyst as the air cathode demonstrated a high open-circuit voltage (1.509 V), high power density (262 mW cm⁻²),

and excellent reversibility and charge-discharge cycling stability, as compared with the ZAB based on a Pt/C air cathode.

Experimental section

Sample preparation

Experimentally, 0.5 g of thiourea and 0.2 g of dopamine were dissolved in 40 mL of deionized water under magnetic stirring, into which were then added 0.2 g of Co(NO₃)₂·6H₂O and 0.2 mL of ethylenediamine. Subsequently, 1.44 mL of formaldehyde solution (38 wt%) was slowly added into the above solution which was stirred at room temperature for 36 h. The obtained intermediate product (denoted as Co-TEFR@PDA) was collected by centrifugation, rinsed extensively with deionized water and ethanol, and dried in an oven at 60 °C for 6 h. The dried powder was then pyrolyzed at 800 °C for 2 h (ramping rate 5 °C min⁻¹) under an Ar/H₂ atmosphere. The resulting product was denoted as Co-NTMCs@NSC.

For comparison, two additional samples were fabricated in the same fashion but without the addition of dopamine or thiourea-formaldehyde, and the corresponding catalysts were denoted as Co@NSC and Co@NC, respectively.

Characterization

Scanning electron microscopy (SEM) measurements were conducted with a field-emission electron microscope (ZEISS, Merlin). Transmission electron microscopy (TEM) measurements were performed on a Tecnai G2-F20 microscope at an applied voltage of 100 kV which was equipped with an energy-dispersive X-ray spectroscopy (EDS) detector. For TEM measurements, a dispersion containing the catalyst was drop-cast directly onto a copper grid coated with an ultrathin amorphous carbon film. X-ray photoelectron spectroscopy (XPS) measurements were performed on a Phi X-tool instrument. Thermogravimetric Analysis (TGA) was performed with a METTLER instrument in air at a heating rate of 5 °C min⁻¹. Powder X-ray diffraction (XRD) patterns were recorded with a Bruker D8-Advance diffractometer using Cu K α radiation. Raman spectra were recorded on a RENISHAW *Via* instrument with an Ar laser source of 488 nm wavelength in a macroscopic configuration. The Brunauer-Emmett-Teller (BET) surface area was determined by using nitrogen isotherms at -196 °C using a Micromeritics ASAP 2010 instrument and the corresponding pore size distributions were calculated by using the Barrett-Joyner-Halenda (BJH) method.

Electrochemistry

Electrochemical measurements were conducted on a CHI 750E electrochemical workstation using a conventional three-electrode cell. A rotating (gold) ring-(glassy carbon) disk electrode (RRDE) was used as the working electrode. A Ag/AgCl electrode (3 M KCl) and a platinum wire were used as the reference and counter electrode, respectively. The Ag/AgCl electrode was calibrated against the reversible hydrogen electrode (RHE), and all potentials in the present study were referred to this RHE. Prior

to electrochemical experiment, 2.0 mg of the as-prepared catalyst was dispersed in 980 μL of ethanol under ultrasonic agitation for 20 min. Subsequently, 20 μL of Nafion (5 wt%) was added into the dispersion under sonication to form a homogeneous ink. A calculated amount of the catalyst ink was then drop-cast onto the surface of the glassy carbon disk electrode (GCE) to form an evenly thin film at a catalyst loading of 0.408 mg cm^{-2} (0.204 mg cm^{-2} for commercial Pt/C). Linear sweep voltammograms (LSVs) were recorded in an O_2 -saturated electrolyte (0.1 M KOH) at various rotation speeds within the range of 400 to 2025 rpm. The number of electron transfer (n) for the ORR was calculated by eqn (1),

$$n = \frac{I_{\text{Disk}}}{I_{\text{Ring}}/N + I_{\text{Disk}}} \quad (1)$$

and the corresponding HO_2^- yield was evaluated by eqn (2),

$$\text{HO}_2^- \% = \frac{200I_{\text{Ring}}/N}{I_{\text{Ring}}/N + I_{\text{Disk}}} \quad (2)$$

where N is the RRDE collection efficiency (37%) and I_{Disk} and I_{Ring} correspond to the voltammetric currents detected at the disk and ring electrode, respectively.

OER measurements were also conducted with the same electrochemical setup but in 1.0 M KOH electrolyte. The catalyst loading on the electrode surface was also 0.408 mg cm^{-2} .

Assembly of rechargeable Zn–Air batteries

Rechargeable Zn–air batteries were assembled by using a zinc plate as the anode and nickel mesh as a current collector, while the bifunctional electrocatalysts loaded on hydrophobic carbon cloth were utilized as the air cathode and diffusion layer. The air cathode was prepared by the following method: 3.0 mg of the catalyst was firstly dispersed into 1.0 mL ethanol solution containing 100.0 μL of Nafion solution (5 wt%) and subjected to ultrasonication treatment for 30 min. Subsequently, the above mixture was drop-cast onto the hydrophobic side of the carbon cloth with an effective catalyst-modified geometric area of 1.0 cm^2 (the corresponding catalyst loading was 2.0 mg cm^{-2}). An electrolyte containing 6 M KOH and 0.2 M $\text{Zn}(\text{Ac})_2 \cdot 2\text{H}_2\text{O}$ was filled between the cathode and anode.

Results and discussion

The synthetic process of Co-NTMCs@NSC electrocatalysts is schematically illustrated in Fig. 1, where Co(II) ion-driven self-assembly of TEFR and PDA is utilized for the synthesis of a precursor that concurrently contains N, S and Co heteroatoms. Experimentally, a given amount of cobaltous nitrate was added to a mixed solution of thiourea and formaldehyde (CH_2O) in the presence of ethylenediamine (EDA), leading to the coprecipitation of Co-TEFR. Meanwhile, the color of the precursor (Co-TEFR@PDA) was between that of Co-TEFR and PDA (Fig. S1†). These observations indicate that TEFR and PDA are successfully assembled in the presence of Co(II) ions.

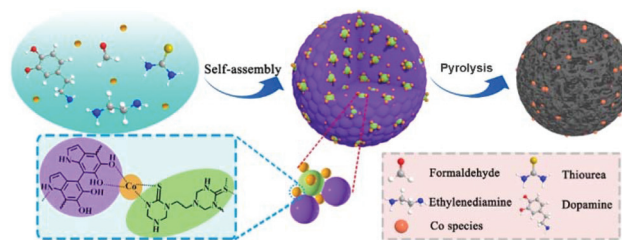


Fig. 1 Schematic illustration of the synthesis of Co-NTMCs@NSC.

The assembly process is supported by the results from FTIR measurements (Fig. S2†), in which Co-TEFR@PDA exhibits several characteristic vibration bands for the Co-TEFR functional groups, such as the C–S stretching at 621 cm^{-1} and C–H vibrations at 1458 cm^{-1} and 2910 cm^{-1} , as well as C=C stretching at 1623 cm^{-1} from PDA, indicating successful assembly of Co-TEFR and PDA. This observation was also confirmed by XPS measurements. In the XPS survey spectra (Fig. S3a†), the presence of Co, O, C, N, and S can be clearly identified in Co-TEFR and Co-TEFR@PDA. Furthermore, in the corresponding high-resolution C 1s spectra (Fig. S3b†), the carbons of C–H (283.8 eV)²³ and C–S (about 285.0 eV) in Co-TEFR and Co-TEFR@PDA can be readily resolved. The absence of C–H (283.8 eV) species in PDA and Co-PDA samples confirmed the successful polymerization of dopamine into PDA. In addition, the C–N peak (285.6 eV) of Co-TEFR@PDA showed a shift of $+0.2$, $+0.4$, and -0.2 eV as compared with those of Co-PDA, PDA and Co-TEFR, respectively. A similar shift of binding energy is also observed for the C–S and C–OH species (about 286.2 eV). These results indicate that self-assembly of TEFR and PDA is induced by the strong chelating interactions between the Co(II) ions (which acted as mediators) and the functional groups with lone-pair electrons (such as HS–, $-\text{NH}_2$, and $-\text{OH}$) on TEFR and PDA to form the Co-TEFR@PDA complex.

Subsequent pyrolysis at $800 \text{ }^\circ\text{C}$ under an Ar/H_2 atmosphere converted the Co-TEFR@PDA precursor to the target product Co-NTMCs@NSC. The as-synthesized Co-NTMCs@NSC was firstly investigated by SEM measurements. As shown in Fig. 2a and b, the Co-NTMCs@NSC sample consisted of a number of rough, porous submicron spheres. Statistical analysis based on more than 200 particles showed that the particle diameter of carbon spheres was about 230 nm, as depicted in the inset of Fig. 2a. In contrast, a compact surface with poor thermal stability was observed for Co@NSC, while a smooth surface was detected for Co@NC (Fig. S4†). Note that the rough surface and porosity of Co-NTMCs@NSC are beneficial to the exposure of active sites and the infiltration of the electrolyte as well as the transport of intermediate products, which can positively influence the electrocatalytic reaction (*vide infra*).^{24–26} In addition, EDS measurements clearly show S element in Co-NTMCs@NSC and Co@NSC (Fig. S5†), signifying that the S atoms were at least partly retained during the pyrolysis process. From the TEM images depicted in Fig. 2c and d, dark-

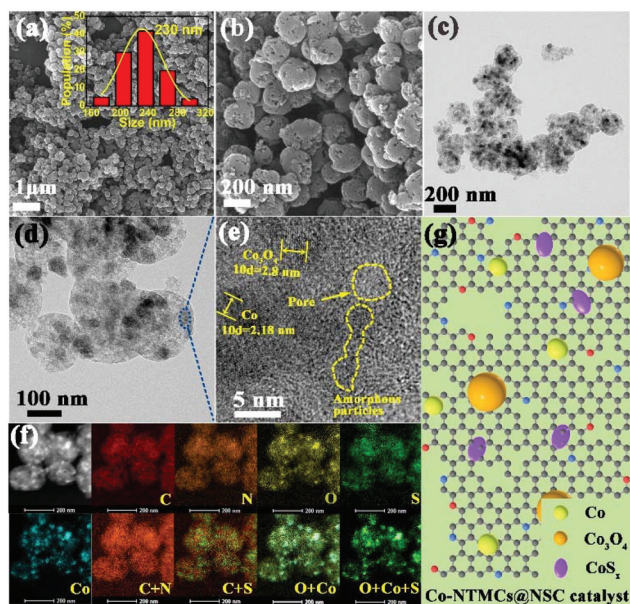


Fig. 2 (a and b) SEM images, (c and d) TEM images, and (e) HR-TEM image of the Co-NTMCs@NSC sample; (f) EDS element mapping of the selected-area image; and (g) schematic image for illustrating different Co-containing species on NSC. The inset in panel (a) is the corresponding diameter size distribution plot of Co-NTMCs@NSC particles.

contrast nanoparticles with an average diameter of tens of nanometers can be observed to be uniformly distributed within the carbon matrix. In the corresponding high-resolution TEM image of the marked region in Fig. 2e, lattice fringes with d -spacings of 0.218 nm and 0.280 nm are clearly observed, which accords well with the (111) planes of metallic Co and (311) planes of Co_3O_4 , respectively.^{16,27} From the elemental maps depicted in Fig. 2f, one can see that N, S and C were uniformly distributed on the entire sample, whereas Co, S and O are somewhat localized on similar spots, suggesting the formation of Co, Co_3O_4 and CoS_x species. Furthermore, the interface between these species and the N, S-doped carbon matrix could be observed in the enlarged high-resolution TEM (HR-TEM) images, as depicted in Fig. S6 and S7.† Correspondingly, the distribution of those Co-NTMCs in the carbon matrix is schematically illustrated in Fig. 2g. In addition, the content of metallic Co in the Co-NTMCs@NSC composite was determined to be 19.5 wt% by TGA measurement (Fig. S8†).

Fig. 3a shows the XRD patterns of the different nanocomposites, where face-centered-cubic (fcc) metallic Co (JCPDS No. 15-0806) was observed in all samples. Meanwhile, crystalline Co_3O_4 and Co_4S_3 were identified in Co-NTMCs@NSC and Co@NSC, respectively. Note that no diffraction peak of CoS_x is observed in Co-NTMCs@NSC, signifying the amorphous nature of CoS_x in the sample.²⁸ Fig. 3b shows the Raman spectra of the series of samples. For carbon materials, the G band at around 1595 cm^{-1} is associated with the E_{2g} mode, while the D band located at about 1324 cm^{-1} corresponds to the structural defects or disordered carbon.²⁹

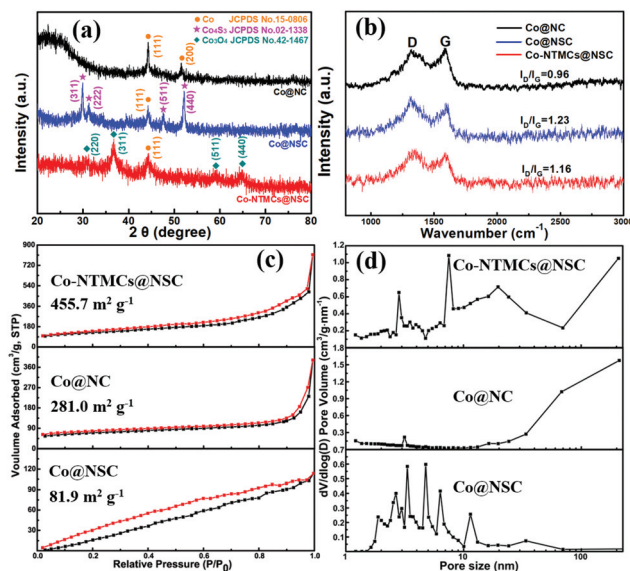


Fig. 3 (a) XRD patterns, (b) Raman spectra, (c) N_2 adsorption/desorption isotherms, and (d) pore size distribution for various samples.

The ratio of the D and G band intensity was estimated to be 1.16 for Co-NTMCs@NSC, which is lower than that of Co@NSC (1.23) but higher than that of Co@NSC (0.96). This implies that Co-TEFR facilitates the formation of defective structures, which may lead to an improvement of the electrocatalytic activity.^{30–32} Furthermore, in the Raman spectra in the low wavenumber region, Co-NTMCs@NSC exhibits several characteristic Raman peaks for Co_3O_4 and CoS_x (Fig. S9†), which suggests the coexistence of Co_3O_4 and CoS_x species, coinciding with the XRD and TEM results.

The BET specific surface area of Co-NTMCs@NSC was measured to be $455.7\text{ m}^2\text{ g}^{-1}$ (Fig. 3c), as listed in Table 1, which is larger than those for Co@NSC ($283.0\text{ m}^2\text{ g}^{-1}$) and Co@NSC ($81.9\text{ m}^2\text{ g}^{-1}$). The Co-NTMCs@NSC sample showed an obvious hysteresis loop in the N_2 adsorption/desorption isotherm, confirming the formation of mesopores. Note that the appearance of rapid N_2 uptake at $P/P_0 > 0.9$ for Co-NTMCs@NSC suggests the formation of secondary, much larger pores, which is different from Co@NSC that is entirely caused by the stacking gap of carbon particles.^{33,34} This observation is consistent with the difference of the morphology and surface texture observed in SEM studies (Fig. 1 and S3†). In addition, the corresponding pore size distribution confirmed the formation of a hierarchical porous structure in Co-NTMCs@NSC, including a broad distribution of mesopores and macropores. This observation signifies the successful assembly of Co-TEFR and PDA, which helps to form a hierarchical porous structure after pyrolysis. Co@NSC and Co-NTMCs@NSC showed a similar pore size distribution, while Co@NSC was predominantly composed of macropores, along with a very small portion of mesopores (Fig. 3d). Note that the presence of abundant mesopores and macropores in Co-NTMCs@NSC is anticipated to remarkably facilitate electrolyte

Table 1 Summary of the specific surface area, predominant pore size and element content of different samples

| Sample name | N ₂ ad-/de-sorption | | Element content determined by XPS | | | | | | | |
|--------------|---|---|-----------------------------------|---------|---------|----------|-------------|------------|-------------|------------|
| | <i>S</i> _{BET} (m ² g ⁻¹) | <i>D</i> _p ^a (nm) | C (at%) | O (at%) | S (at%) | Co (at%) | N (at%) | | | |
| | | | | | | | Pyridinic N | Pyrrolic N | Graphitic N | Oxidized N |
| Co@NC | 281.0 | >50 | 91.60 | 3.80 | 0.08 | 0.50 | 0.9 | — | 2.21 | 0.89 |
| Co@NSC | 81.9 | 3.3–11.5 | 57.40 | 18.66 | 15.01 | 2.12 | 1.25 | 4.75 | 0.81 | — |
| Co-NTMCs@NSC | 455.7 | 2.8–20; >50 | 86.93 | 6.19 | 1.57 | 0.77 | 0.71 | — | 3.83 | — |

^a *D*_p denotes the predominant pore size determined by the BJH model.

diffusion and kinetic accessibility of the active sites, respectively, as detailed below.

XPS measurements were conducted to analyze the elemental composition and bonding configuration in Co-NTMCs@NSC. From the survey spectrum in Fig. 4a, the C, N, O, S and Co elements can be readily identified, consistent with the results of EDS measurements (Fig. S5[†]). The high-resolution C 1s spectrum (Fig. 4b) can be deconvoluted into five peaks corresponding to C=C-C (284.6 eV), C-S (285 eV), C-N (285.6 eV), C-O (287.4 eV) and C=O (290.0 eV), indicating the incorporation of N and S heteroatoms in the hybrid.^{35,36} The high-resolution N 1s spectrum in Fig. 4c can be fitted into two peaks centered at 398.6 and 401.0 eV, corresponding to pyridinic-N and graphitic-N, respectively. Recently, we have demonstrated that graphitic N is most likely responsible for the ORR catalytic activities of nitrogen-doped carbons in alkaline elec-

trolytes.³⁷ Therefore, the presence of a high content of graphitic-N in Co-NTMCs@NSC is shown in Table 1, which is beneficial to improve its ORR electrocatalysis. Fig. 4d shows the high-resolution O 1s spectrum, which can be deconvoluted into Co-O (530.7 eV), C=O (531.7 eV), C-O-C (532.6 eV) and C-OH (533.5 eV), consistent with the formation of cobalt oxide nanoparticles. Besides, the high-resolution S 2p spectrum can be deconvoluted into four species at 162.3 (Co-S), 164.2 eV (C-S), 165.5 eV (C=S) and 168.8 eV (S-O) (Fig. 4e), indicating successful doping of S element into the carbon skeleton and the concurrent formation of metal sulfide during pyrolysis. In Fig. 4f, the high-resolution Co spectrum is fitted into four peaks, corresponding to Co⁰, Co-O, Co-S and the shake-up (satellites) peaks. The peaks centered at about 781.1 and 796.7 eV most likely arose from Co-O. The observation of satellite peaks at higher binding energies of 784.8 and 803.9 eV revealed the presence of antibonding orbitals between Co and O atoms and hence further confirmed the presence of cobalt oxide species in the composite.³⁸ More importantly, this phenomenon also suggests that the electronic configuration of Co is close to t_{2g}⁶e_g¹, which is near the optimal e_g filling, and effectively promotes the breaking of the M-OH⁻ bond as well as the O₂²⁻/OH⁻ exchange reaction, hence favorable for high electrocatalytic activity towards the ORR.³⁹ The peaks at 778.2 eV and 793.2 eV are assigned to metallic Co.¹ Furthermore, the peak at 778.9 eV is attributed to the Co-S bond, consistent with the results from high-resolution S 2p scan and elemental mapping measurements (Fig. 2). Taken together, these results signify the formation of Co⁰, Co₃O₄ and CoS_x nanoparticles in the Co-NTMCs@NSC composite.

To investigate the electrocatalytic performance of Co-NTMCs@NSC, cyclic voltammetry (CV) measurements were first carried out in an O₂ or N₂-saturated 0.1 M aqueous KOH solution. As shown in Fig. 5a, a characteristic oxygen reduction peak was observed at +0.844 V (vs. RHE) for Co-NTMCs@NSC in O₂-saturated 0.1 M aqueous KOH, in comparison with the featureless profile observed under N₂ saturation, indicative of considerable ORR activity of Co-NTMCs@NSC. Linear sweep voltammogram (LSV) measurements were then performed on Co-NTMCs@NSC, Co@NSC, and Co@NC samples using an RRDE at 1600 rpm. As displayed in Fig. 5b, the Co-NTMCs@NSC catalyst shows an onset potential of +0.945 V, which is much more positive than those of Co@NSC (+0.842 V) and Co@NC (+0.873 V) and is close to that of the commercial Pt/C catalyst

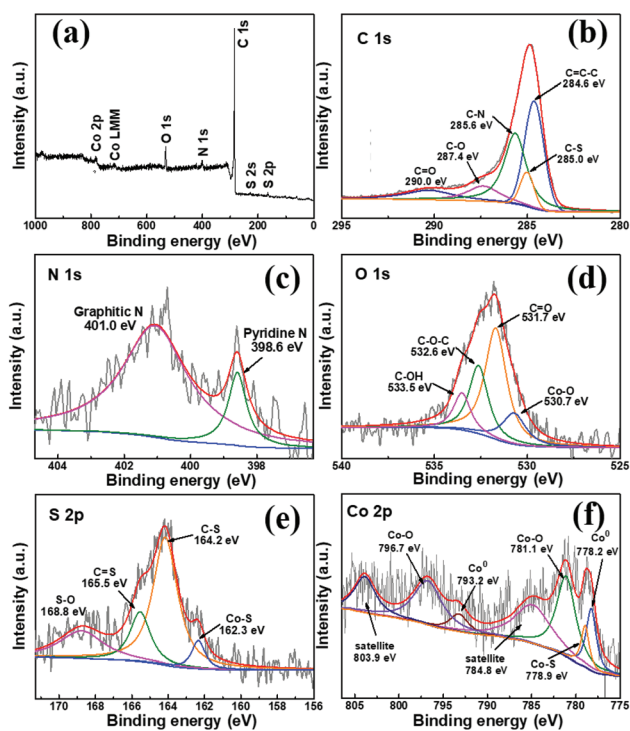


Fig. 4 (a) XPS survey spectrum and the corresponding high-resolution spectra of (b) C 1s, (c) N 1s, (d) O 1s, (e) S 2p and (f) Co 2p of the Co-NTMCs@NSC sample.

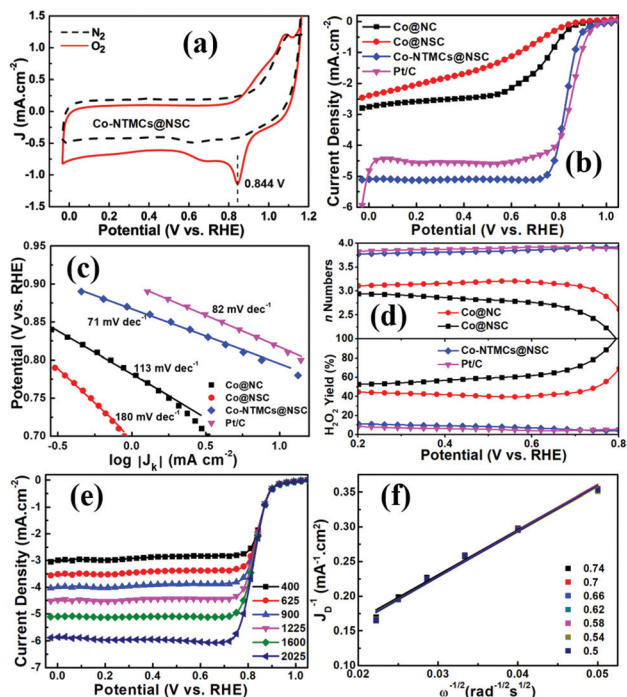


Fig. 5 (a) CVs of Co-NTMCs@NSC in an O₂ and N₂-saturated 0.1 M KOH aqueous solution. (b) LSVs of different samples determined at 1600 rpm with a sweep scan of 5 mV s⁻¹. (c) The corresponding Tafel plots of different catalysts. (d) The plots of the number of electron transfer and the corresponding HO₂⁻ yield of a GCE loaded with different catalysts determined at an electrode rotation speed of 1600 rpm. (e) LSVs for Co-NTMCs@NSC at a rotating speed varying between 400 and 2025 rpm and (f) the correlated K–L plots.

(+0.956 V). In terms of half wave potential, the value of Co-NTMCs@NSC (+0.833 V) is also very close to that of the commercial Pt/C catalyst (+0.854 V). Meanwhile, the limiting current density of Co-NTMCs@NSC reaches 5.11 mA cm⁻², which is much higher than that observed for commercial Pt/C. Similarly, from the corresponding linear fittings of the Tafel plots (Fig. 5c), the slope was determined to be 74 mV dec⁻¹ for Co-NTMCs@NSC, 180 mV dec⁻¹ for Co@NSC, 113 mV dec⁻¹ for Co@NC, and 82 mV dec⁻¹ for Pt/C, which signifies that the rate-determining step for the ORR on the Co-NTMCs@NSC catalyst is similar to that on Pt/C, *i.e.*, the first-electron reduction of oxygen. Fig. 5d displays the plots of electron-transfer number *n* against sweeping potential, where Co-NTMCs@NSC shows an electron-transfer number of almost 4 in a wide range of potential from +0.9 to +0.0 V. Specifically, the *n* value of N,S-Co@NC is calculated to be 3.90 at +0.700 V, comparable to that (3.91) of Pt/C, but significantly higher than those for N,S-Co@C (2.60) and for Co@NC (3.12), signifying a high selectivity towards the preferred 4e⁻ pathway for ORR electrocatalysis on Co-NTMCs@NSC. This conclusion is also supported by a peroxide species yield of about 9.0% observed for Co-NTMCs@NSC (Fig. 5d), lower than the 57.5% for Co@NSC and 41.0% for Co@NC samples and even comparable to the 6.0% value of the Pt/C catalyst. In addition, LSVs were

also recorded at a varied electrode rotation speed between 400 and 2025 rpm to examine the reaction selectivity of Co-NTMCs@NSC (Fig. 5e). The limiting current density gradually increases with increasing rotation speed. The corresponding Koutecky–Levich (K–L) plots for all samples are shown in Fig. 5f and Fig. S10,† where excellent linearity can be seen within a potential range of +0.50 and +0.74 V, with a nearly identical slope value, suggesting a first order reaction kinetics with respect to the concentration of dissolved oxygen.

Operational stability is of paramount importance in catalysis. Fig. S11† depicts the chronoamperometric profiles of commercial Pt/C and Co-NTMCs@NSC at an applied potential of +0.50 V, where one can find that after continuous operation for 40 000 s, the voltammetric current of the benchmark Pt/C-modified electrode decreased to about 71.6% of the initial value, while 93.4% of the current was retained for the Co-NTMCs@NSC-modified electrode. These observations clearly demonstrate that Co-NTMCs@NSC has higher operational stability than commercial Pt/C in ORR electrocatalysis.

The tolerance to fuel crossover is another important issue for ORR catalysts in practical applications. Herein, we used methanol, a common fuel in fuel cells, as an illustrating example to conduct comparison studies. As shown in Fig. S12,† the current density of the Pt/C electrode exhibits a significant decrease upon the addition of 1 M methanol, whereas no noticeable change was observed for the Co-NTMCs@NSC electrode. This demonstrates that Co-NTMCs@NSC possesses excellent tolerance to methanol crossover.

Interestingly, the above Co-NTMCs@NSC composites also exhibit apparent activity towards the OER, and thus may be used as a bifunctional electrocatalyst for the air cathode of rechargeable metal–air batteries.⁴⁰ As shown in Fig. 6a, a sudden increase of voltammetric currents in the linear polarization curves was observed in the positive potential sweep from +1.050 to +1.800 V for all carbon catalysts prepared above, signifying a considerable OER catalytic activity. Specifically, to reach a current density of 10 mA cm⁻², an electrode potential (*E*_{OER,10}) of +1.514 V was required for Co-NTMCs@NSC, which is much lower than the +1.655 V for Co@NC, +1.623 V for Co@NSC, and +1.546 V for RuO₂, indicating that Co-NTMCs@NSC possesses the highest OER catalytic activity among the series. In the corresponding Tafel plots (Fig. 6b), a large slope of 161 mV dec⁻¹ was identified for the Co@NC catalyst, which decreased markedly to 132 mV dec⁻¹ for Co@NSC, and further to 101 mV dec⁻¹ for Co-NTMCs@NSC. Note that the later was comparable to that of RuO₂ (92 mV dec⁻¹), suggesting a good kinetics and bubble-releasing ability of Co-NTMCs@NSC. In the electrochemical impedance spectra depicted in Fig. 6c, Co-NTMCs@NSC can be seen to display a smaller semicircle than Co@NC, Co@NSC, and even RuO₂ at +1.550 V, signifying that the activation energy of the OER on Co-NTMCs@NSC was the lowest among the series of samples.

Chronoamperometric measurements were further conducted to evaluate the OER stability of Co-NTMCs@NSC, as compared with RuO₂. From Fig. 6d, it is obviously found that the current of the RuO₂-modified electrode decayed to 31% of

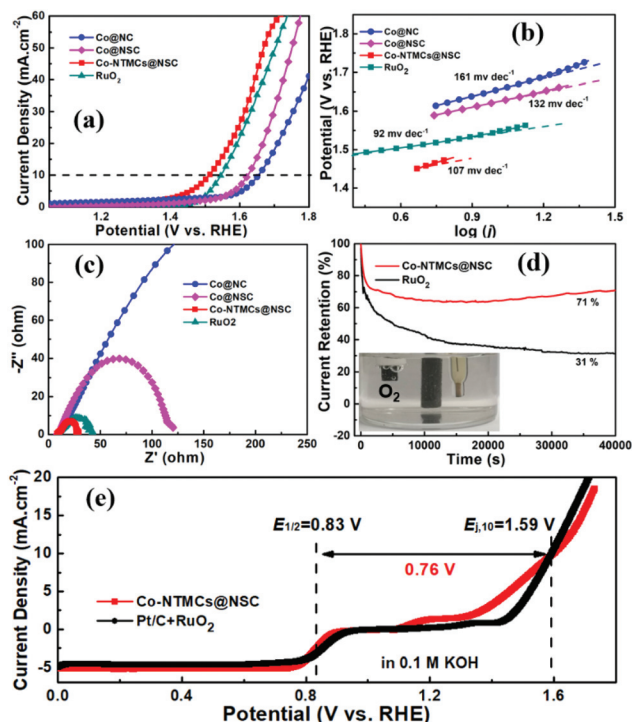


Fig. 6 (a) OER LSVs of the different samples at 1600 rpm with a sweep scan of 10 mV s^{-1} in 1.0 M KOH electrolyte. (b) The corresponding Tafel plots derived from OER polarization curves. (c) EIS curves for Co@NC, Co@NSC, Co-NTMCs@NSC, and RuO_2 at $+1.550 \text{ V vs. RHE}$ with an AC amplitude of 5 mV from the frequency range of 10 kHz to 0.01 Hz . (d) Long-term stability of Co-NTMCs@NSC and commercial RuO_2 catalysts in OER electrocatalysis. The inset in panel (d) is the optical photo showing bubble accumulation on carbon cloth loaded with the Co-NTMCs@NSC catalyst during OER measurement. (e) Overall polarization curves of Co-NTMCs@NSC and Pt/C + RuO_2 catalysts in 0.1 M KOH electrolyte. The bifunctional ORR/OER activity is evaluated by the potential difference (ΔE) between the half-wave potential for the ORR and the metric potential at 10 mA cm^{-2} for the OER.

its initial value after continuous operation for $40\,000 \text{ s}$, while 71% was retained for Co-NTMCs@NSC. The above results suggest that Co-NTMCs@NSC might serve as a highly active electrocatalyst for both the ORR and OER. In addition, the bifunctional catalytic activities can be evaluated by the potential gap ($\Delta E = E_{j,10} - E_{1/2}$) between the $E_{1/2}$ for the ORR and the potential to reach a current density of 10 mA cm^{-2} ($E_{j,10}$) for the OER, where a smaller ΔE signifies a more reversible oxygen electrode. As depicted in Fig. 6e, Co-NTMCs@NSC exhibits the smallest ΔE value of 0.76 V , which is better than that of most bifunctional catalysts and even approximately close to that of commercial Pt/C and RuO_2 electrodes (Table S1†).

To study the effects of Co-containing species in the Co-NTMCs@NSC catalyst on ORR and OER electrocatalysis, the Co, Co_3O_4 and CoS_x nanoparticles were removed by acid washing ($0.5 \text{ M H}_2\text{SO}_4$ at $80 \text{ }^\circ\text{C}$). As shown in Fig. S13a,† after acid washing, the half-wave potential is negatively shifted by 33 mV and the limiting current density significantly decreases in the ORR polarization curves, confirming a clear deterior-

ation of the ORR activity. Similarly, after acid treatment a positive shift of 170 mV is also observed in the OER LSV curves depicted in Fig. S13b.† This result clearly indicated that the Co-containing nanoparticle species were responsible for the remarkable ORR/OER activity of Co-NTMCs@NSC. Previous studies have demonstrated that the ORR could be catalyzed by Co, N codoped carbons, Co and Co_3O_4 species,^{11,41–43} while Co_3O_4 and CoS_x nanoparticles contribute to the OER activity.^{17,44–47} Yet, the ORR and OER can also be catalyzed by defects and carbon atoms adjacent to heteroatoms, such as N and S, in carbon skeletons.^{48,49} Based on the above analysis, it is most likely the synergistic effect between the heteroatom codoped carbon framework, hierarchical porosity, defective structures and Co-containing species that contributed to the high ORR/OER catalytic activities of Co-NTMCs@NSC.

The application of Co-NTMCs@NSC in rechargeable Zn–air batteries was then tested. Zinc foil was used as the anode, catalyst-modified carbon cloth was used as the air cathode, and an aqueous solution containing $6.0 \text{ M KOH} + 0.2 \text{ M}$ zinc acetate was utilized as the working electrolyte, as depicted in Fig. 7a. Fig. 7b reveals that a high open-circuit voltage of 1.509 V (inset of panel b) is observed for the battery with a Co-NTMCs@NSC

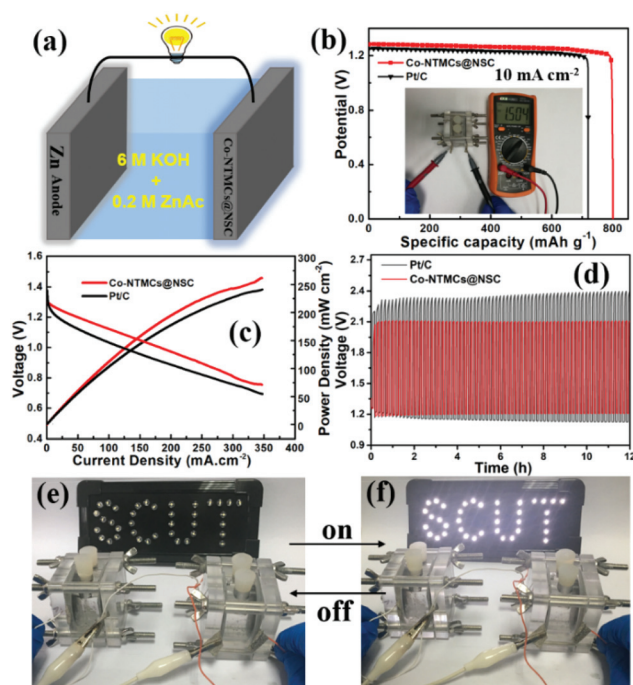


Fig. 7 (a) Schematic diagram of a rechargeable Zn–air battery. (b) Specific capacities for Zn–air batteries normalized to the consumed mass of Zn at a discharged current density of 10 mA cm^{-2} . The inset in panel (b) is a photograph showing the open circuit voltage of the Zn–air battery. (c) The plots of discharged voltage and corresponding power density against current density for Zn–air batteries employing Co-NTMCs@NSC or Pt/C modified air cathodes. (d) Zn–air batteries continuously running charge–discharge cycle at 10 mA cm^{-2} . Both the discharge and charge intervals were set for 5 minutes . LEDs (e) before and (f) after being lit by two Co-NTMCs@NSC Zn–air batteries connected in series.

air cathode, and the corresponding specific capacity normalized to the weight of the consumed zinc plate is determined to be 800 mA h g^{-1} at 10 mA cm^{-2} , higher than that of Pt/C (719 mA h g^{-1} at 10 mA cm^{-2}). Furthermore, from the discharge profiles in Fig. 7c, it is clearly found that the Co-NTMCs@NSC-based battery shows a higher discharge voltage than that with Pt/C at different current densities (e.g., 1.12 V vs. 1.03 V at 100 mA cm^{-2}). Moreover, the battery with a Co-NTMCs@NSC air cathode exhibited a maximum power density of 262 mW cm^{-2} , also much higher than that of the battery with Pt/C (241 mW cm^{-2}). Fig. 7d depicts the voltage evolution of the two batteries during charge–discharge cycling processes. At the beginning, the charge–discharge voltage gap is about 0.805 V for the Co-NTMCs@NSC battery, much lower than that (0.936 V) for the Pt/C one. After a continuous galvanostatic charge–discharge measurement for 12 h, the charge–discharge voltage gap was slightly increased to about 0.897 V for the former, while a significantly larger value of 1.270 V was observed for the latter, indicative of a superior operational stability of Co-NTMCs@NSC serving as the breathing air-cathode in rechargeable Zn–air batteries. As a demonstration of real applications (Fig. 7e–f), a series of LEDs (the working voltage for each LED is about 3.0 V) can be lit by only two Co-NTMCs@NSC Zn–air batteries connected in series.

Conclusion

In summary, nitrogen and sulfur co-doped porous carbon spheres embedded with Co-containing nanoparticles were successfully synthesized by using Co-TEFR as a pore-forming agent and a multi-heteroatom source to dope heteroatoms into the carbon matrix and generate hierarchical porous textures. The resulting Co-NTMCs@NSC catalyst comprised abundant active sites (defective sites and carbon atoms adjacent to heteroatoms) in the skeletons and possessed multiple Co-containing catalytically active species, as well as their synergistic interactions for boosting the ORR/OER activities. As for ORR electrocatalysis, Co-NTMCs@NSC displayed a half-wave potential of $+0.833 \text{ V}$, nearly four-electron reduction selectivity, together with a high limiting current density, excellent methanol tolerant ability and long-term durability in alkaline medium, as compared with the commercial Pt/C catalyst. In addition, it also exhibited an efficient OER catalytic activity, featuring an overpotential of 284 mV at 10 mA cm^{-2} , and high working durability; both are better than those of the commercial RuO_2 catalyst. When loaded on the air cathode of a rechargeable Zn–air battery, the Co-NTMCs@NSC-based device showed a higher open-circuit voltage of 1.509 V , higher power density (262 mW cm^{-2}) and much smaller charge–discharge voltage gap during 12 h of charge–discharge cycling, as compared with the reference device with a Pt/C-based air cathode. This work may provide a novel avenue to the synthesis of transition-metal-containing, hierarchically porous, doped carbon composites that can serve as high-performance electrocatalysts for electrochemical energy technologies.

Conflicts of interest

There are no conflicts to declare.

Acknowledgements

We gratefully acknowledge the financial support from the National Key R&D Program of China (2018YFB1502600), the National Natural Science Foundation of China (NSFC 51402111 and 21528301), the Fundamental Research Funds for the Central Universities (SCUT Grant No. 2018ZD21) and Open Research Fund of State Key Laboratory of Polymer Physics and Chemistry, Changchun Institute of Applied Chemistry, Chinese Academy of Sciences.

References

- 1 T. Li, Y. Lu, S. Zhao, Z.-D. Gao and Y.-Y. Song, *J. Mater. Chem. A*, 2018, **6**, 3730–3737.
- 2 Q. Wang, Z. Zhang, M. Wang, F. Liu, L. Jiang, B. Hong, J. Li and Y. Lai, *Nanoscale*, 2018, **10**, 15819–15825.
- 3 X. X. Wang, D. A. Cullen, Y.-T. Pan, S. Hwang, M. Wang, Z. Feng, J. Wang, M. H. Engelhard, H. Zhang, Y. He, Y. Shao, D. Su, K. L. More, J. S. Spendelow and G. Wu, *Adv. Mater.*, 2018, **30**, 1706758.
- 4 C.-Y. Su, H. Cheng, W. Li, Z.-Q. Liu, N. Li, Z. Hou, F.-Q. Bai, H.-X. Zhang and T.-Y. Ma, *Adv. Energy Mater.*, 2017, **7**, 1602420.
- 5 N. Wang, L. Li, D. Zhao, X. Kang, Z. Tang and S. Chen, *Small*, 2017, **13**, 1701025.
- 6 W. Niu, S. Pakhira, K. Marcus, Z. Li, J. L. Mendoza-Cortes and Y. Yang, *Adv. Energy Mater.*, 2018, **8**, 1800480.
- 7 Y. Lu, S. Zhao, R. Yang, D. Xu, J. Yang, Y. Lin, N. E. Shi, Z. Dai, J. Bao and M. Han, *ACS Appl. Mater. Interfaces*, 2018, **10**, 8155–8164.
- 8 T. Wang, R. Yang, N. Shi, J. Yang, H. Yan, J. Wang, Z. Ding, W. Huang, Q. Luo, Y. Lin, J. Gao and M. Han, *Small*, 2019, 1902410.
- 9 S. Zhao, M. Li, M. Han, D. Xu, J. Yang, Y. Lin, N.-E. Shi, Y. Lu, R. Yang, B. Liu, Z. Dai and J. Bao, *Adv. Funct. Mater.*, 2018, **28**, 1706018.
- 10 D. Zhao, L. Li, L. Xie, N. Zhou and S. Chen, *J. Alloys Compd.*, 2018, **741**, 368.
- 11 Y. Niu, X. Huang, X. Wu, L. Zhao, W. Hu and C. Ming Li, *Nanoscale*, 2017, **9**, 10233–10239.
- 12 W. Wei, H. Liang, K. Parvez, X. Zhuang, X. Feng and K. Müllen, *Angew. Chem., Int. Ed.*, 2014, **53**, 1570–1574.
- 13 W. Han, L. Li and S. Chen, *J. Electrochem.*, 2017, **23**, 110.
- 14 J. Zhang, G. Chen, K. Müllen and X. Feng, *Adv. Mater.*, 2018, **30**, 1800528.
- 15 Y. Jia, L. Zhang, A. Du, G. Gao, J. Chen, X. Yan, C. L. Brown and X. Yao, *Adv. Mater.*, 2016, **28**, 9532–9538.
- 16 X. Zhang, R. Liu, Y. Zang, G. Liu, G. Wang, Y. Zhang, H. Zhang and H. Zhao, *Chem. Commun.*, 2016, **52**, 5946–5949.

- 17 X. Han, G. He, Y. He, J. Zhang, X. Zheng, L. Li, C. Zhong, W. Hu, Y. Deng and T.-Y. Ma, *Adv. Energy Mater.*, 2018, **8**, 1702222.
- 18 K. Fan, H. Zou, Y. Lu, H. Chen, F. Li, J. Liu, L. Sun, L. Tong, M. F. Toney, M. Sui and J. Yu, *ACS Nano*, 2018, **12**, 12369–12379.
- 19 X. Wang, J. Wang, D. Wang, S. Dou, Z. Ma, J. Wu, L. Tao, A. Shen, C. Ouyang, Q. Liu and S. Wang, *Chem. Commun.*, 2014, **50**, 4839–4842.
- 20 M. Wu, J. Wang, Z. Wu, H. L. Xin and D. Wang, *J. Mater. Chem. A*, 2015, **3**, 7727–7731.
- 21 J. Chen, H. Zhang, P. Liu, G. Li, T. An and H. Zhao, *Carbon*, 2015, **92**, 339–347.
- 22 S. H. Lee, J. Kim, D. Y. Chung, J. M. Yoo, H. S. Lee, M. J. Kim, B. S. Mun, S. G. Kwon, Y.-E. Sung and T. Hyeon, *J. Am. Chem. Soc.*, 2019, **141**, 2035–2045.
- 23 J. S. Fang, C. S. Lin, Y. Y. Huang and T. S. Chin, *J. Electron. Mater.*, 2015, **44**, 2908–2914.
- 24 W. Niu, L. Li, N. Wang, S. Zeng, J. Liu, D. Zhao and S. Chen, *J. Mater. Chem. A*, 2016, **4**, 10820–10827.
- 25 G. Wang, Y. Sun, D. Li, H.-W. Liang, R. Dong, X. Feng and K. Müllen, *Angew. Chem., Int. Ed.*, 2015, **54**, 15191–15196.
- 26 H.-W. Liang, X. Zhuang, S. Brüller, X. Feng and K. Müllen, *Nat. Commun.*, 2014, **5**, 4973.
- 27 H. Kim, D.-H. Seo, S.-W. Kim, J. Kim and K. Kang, *Carbon*, 2011, **49**, 326–332.
- 28 W. Niu, Z. Li, K. Marcus, L. Zhou, Y. Li, R. Ye, K. Liang and Y. Yang, *Adv. Energy Mater.*, 2018, **8**, 1701642.
- 29 Q. Xiang, W. Yin, Y. Liu, D. Yu, X. Wang, S. Li and C. Chen, *J. Mater. Chem. A*, 2017, **5**, 24314–24320.
- 30 Y. Lin, L. Yang, Y. Zhang, H. Jiang, Z. Xiao, C. Wu, G. Zhang, J. Jiang and L. Song, *Adv. Energy Mater.*, 2018, **8**, 1703623.
- 31 Y. Jia, L. Zhang, A. Du, G. Gao, J. Chen, X. Yan, C. L. Brown and X. Yao, *Adv. Mater.*, 2016, **28**, 9532–9538.
- 32 W. Wang, Y. Liu, J. Li, J. Luo, L. Fu and S. Chen, *J. Mater. Chem. A*, 2018, **6**, 14299–14306.
- 33 X. Zhu, S. Wang, W. Huang, Y. Tian and X. Wang, *Carbon*, 2016, **105**, 521–528.
- 34 X. Zhu, J. Chong, T. Hu, X. Wang and Y. Tian, *J. Mater. Chem. A*, 2017, **5**, 8297–8306.
- 35 X.-R. Wang, J.-Y. Liu, Z.-W. Liu, W.-C. Wang, J. Luo, X.-P. Han, X.-W. Du, S.-Z. Qiao and J. Yang, *Adv. Mater.*, 2018, **30**, 1800005.
- 36 D. Guo, R. Shibuya, C. Akiba, S. Saji, T. Kondo and J. Nakamura, *Science*, 2016, **351**, 361.
- 37 N. Wang, B. Lu, L. Li, W. Niu, Z. Tang, X. Kang and S. Chen, *ACS Catal.*, 2018, **8**, 6827–6836.
- 38 W. Xia, R. Zou, L. An, D. Xia and S. Guo, *Energy Environ. Sci.*, 2015, **8**, 568–576.
- 39 H. Zhong, K. H. Ly, M. Wang, Y. Krupskaya, X. Han, J. Zhang, J. Zhang, V. Kataev, B. Büchner, I. M. Weidinger, S. Kaskel, P. Liu, M. Chen, R. Dong and X. Feng, *Angew. Chem.*, 2019, **131**, 10787–10792.
- 40 F. Cheng and J. Chen, *Chem. Soc. Rev.*, 2012, **41**, 2172–2192.
- 41 Y. Liang, Y. Li, H. Wang, J. Zhou, J. Wang, T. Regier and H. Dai, *Nat. Mater.*, 2011, **10**, 780.
- 42 H. Wang, W. Wang, M. Asif, Y. Yu, Z. Wang, J. Wang, H. Liu and J. Xiao, *Nanoscale*, 2017, **9**, 15534–15541.
- 43 C. Wang, Z. Zhao, X. Li, R. Yan, J. Wang, A. Li, X. Duan, J. Wang, Y. Liu and J. Wang, *ACS Appl. Mater. Interfaces*, 2017, **9**, 41273–41283.
- 44 P. Cai, J. Huang, J. Chen and Z. Wen, *Angew. Chem., Int. Ed.*, 2017, **56**, 4858–4861.
- 45 H.-C. Li, Y.-J. Zhang, X. Hu, W.-J. Liu, J.-J. Chen and H.-Q. Yu, *Adv. Energy Mater.*, 2018, **8**, 1702734.
- 46 H. Jin, J. Wang, D. Su, Z. Wei, Z. Pang and Y. Wang, *J. Am. Chem. Soc.*, 2015, **137**, 2688–2694.
- 47 M. Zhang, Q. Dai, H. Zheng, M. Chen and L. Dai, *Adv. Mater.*, 2018, **30**, 1705431.
- 48 Q. Wang, Y. Ji, Y. Lei, Y. Wang, Y. Wang, Y. Li and S. Wang, *ACS Energy Lett.*, 2018, **3**, 1183–1191.
- 49 H. Jiang, J. Gu, X. Zheng, M. Liu, X. Qiu, L. Wang, W. Li, Z. Chen, X. Ji and J. Li, *Energy Environ. Sci.*, 2019, **12**, 322–333.